

Launching magnons at the terahertz speed of the spin Seebeck effect

T. Seifert¹, S. Jaiswal^{2,3}, J. Barker⁴, I. Razdolski¹, J. Cramer², O. Gueckstock¹, S. Watanabe⁵, C. Ciccarelli⁶, A. Melnikov^{1,7}, G. Jakob², S.T.B. Goennenwein⁸, G. Woltersdorf⁷, P.W. Brouwer⁹, M. Wolf¹, M. Kläui², T. Kampfrath^{1,9}

1. Department of Physical Chemistry, Fritz Haber Institute of the Max Planck Society, 14195 Berlin, Germany
2. Institute of Physics, Johannes Gutenberg University, 55128 Mainz, Germany
3. Singulus Technologies AG, 63796 Kahl am Main, Germany
4. Institute for Materials Research, Tohoku University, Sendai 980-8577, Japan
5. Department of Advanced Materials Science, School of Frontier Sciences, University of Tokyo, Chiba 277-8561, Japan
6. Cavendish Laboratory, University of Cambridge, CB3 0HE Cambridge, United Kingdom
7. Institute of Physics, Martin-Luther-Universität Halle, 06120 Halle, Germany
8. Institute of Structural Physics, Technische Universität Dresden, 01062 Dresden, Germany
9. Department of Physics, Freie Universität Berlin, 14195 Berlin, Germany

* Email: tobias.kampfrath@fu-berlin.de

Transport of spin angular momentum is an essential operation in spintronic devices. In magnetic insulators, spin currents are carried by magnons and can be launched straightforwardly by heating an adjacent metal layer. Here, we study the ultimate speed of this spin Seebeck effect with 10-fs time resolution in prototypical bilayers of ferrimagnetic yttrium iron garnet and platinum. Upon exciting the metal by a laser pulse, the spin flow is measured using the inverse spin Hall effect and terahertz electrooptic sampling. The spin Seebeck current reaches its peak within ~ 200 fs, a hallmark of the photoexcited metal electrons approaching a Fermi-Dirac distribution. Analytical modeling shows the spin Seebeck response is virtually instantaneous because the ferrimagnetic spins react without inertia and the metal spins impinging on the interface have a correlation time of only ~ 4 fs. Novel applications for material characterization, interface probing, spin-noise detection and terahertz spin pumping emerge.

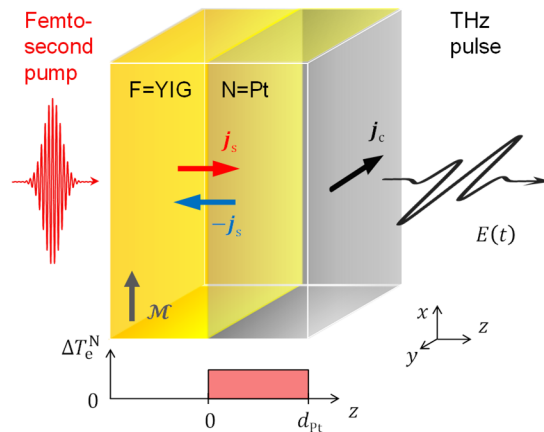


Figure 1 | Schematic of the experiment. To probe the ultimate speed of the spin Seebeck effect, a femtosecond laser pulse (duration 10 fs, center photon energy 1.5 eV) is incident onto a F|N bilayer made of platinum (N=Pt, thickness of $d_{Pt} = 5$ nm) on top of yttrium iron garnet (F=YIG, 5 μ m, in-plane magnetization \mathcal{M}). While the YIG film is transparent to the pump pulse (band gap of 2.6 eV), the Pt film is excited homogeneously, resulting in a transient increase of its electronic temperature ΔT_e^N following thermalization. Any ultrafast spin-current density $j_s(t)$ arising in Pt is converted into a transverse charge-current density $j_c(t)$ by the inverse spin Hall effect, thereby acting as a source of a THz electromagnetic pulse whose transient electric field $E(t)$ is detected by electrooptic sampling.

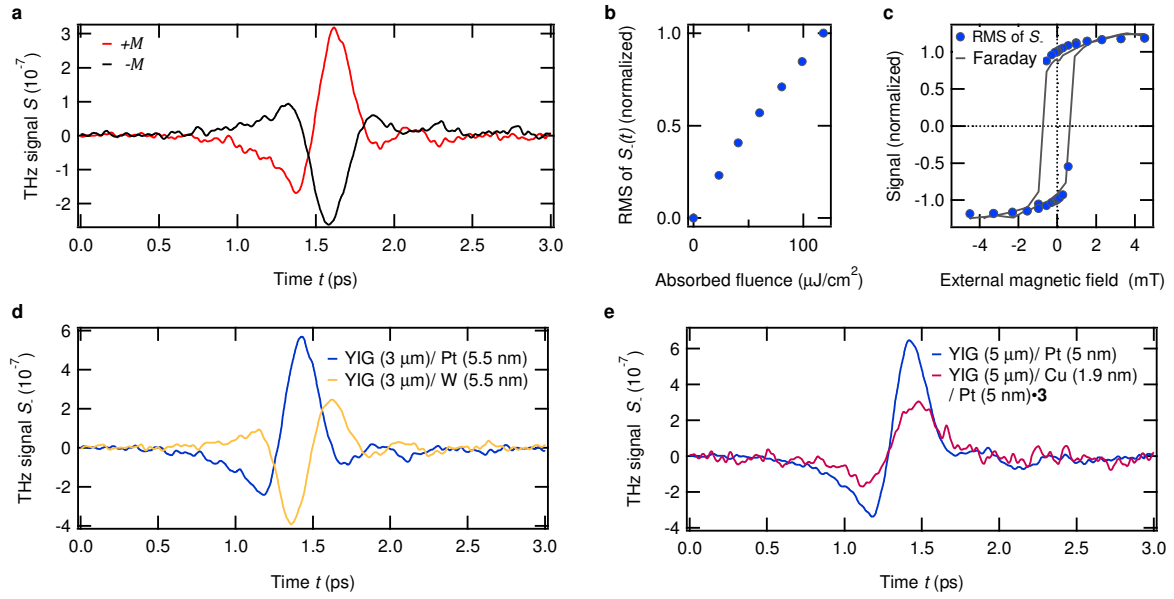


Figure 2 | Terahertz emission of photoexcited F/N bilayers. **a**, THz emission signals $S(\pm\mathcal{M})$ from a YIG(3 μm)|Pt(5.5 nm) sample for opposite directions of the in-plane YIG magnetization \mathcal{M} as a function of time t . We focus on the difference $S_- = S(+\mathcal{M}) - S(-\mathcal{M})$ odd in \mathcal{M} . **b**, Amplitude of S_- (root-mean-square, RMS) as a function of the absorbed pump fluence. **c**, THz signal amplitude (RMS of S_-) and Faraday rotation of a continuous-wave laser beam (wavelength of 532 nm) as a function of the external magnetic field. Both hysteresis loops were measured under identical pump conditions at room temperature. **d**, Terahertz emission signal from a 3 μm thick YIG film capped with platinum (Pt) and tungsten (W), both 5.5 nm thick. **e**, Terahertz emission signal from a 5 μm YIG film capped with 5 nm Pt and with a bilayer of 1.9 nm Cu and 5.4 nm Pt (multiplied by 3).

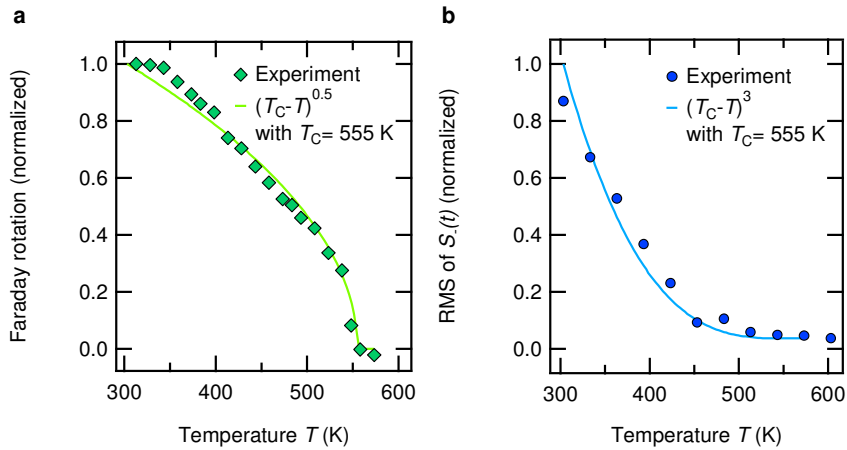


Figure 3 | Impact of sample temperature. **a**, Faraday rotation of a continuous-wave laser beam (wavelength of 532 nm) as a function of the sample temperature. A fit analogous to Ref. 26 reveals a critical exponent of 0.5 and a Curie temperature of $T_C = 555$ K. **b**, Temperature dependence of the magnetic terahertz emission signal. The solid line is a curve $\propto (T - T_C)^3$, exactly as used in previous work on the DC SSE²⁶.

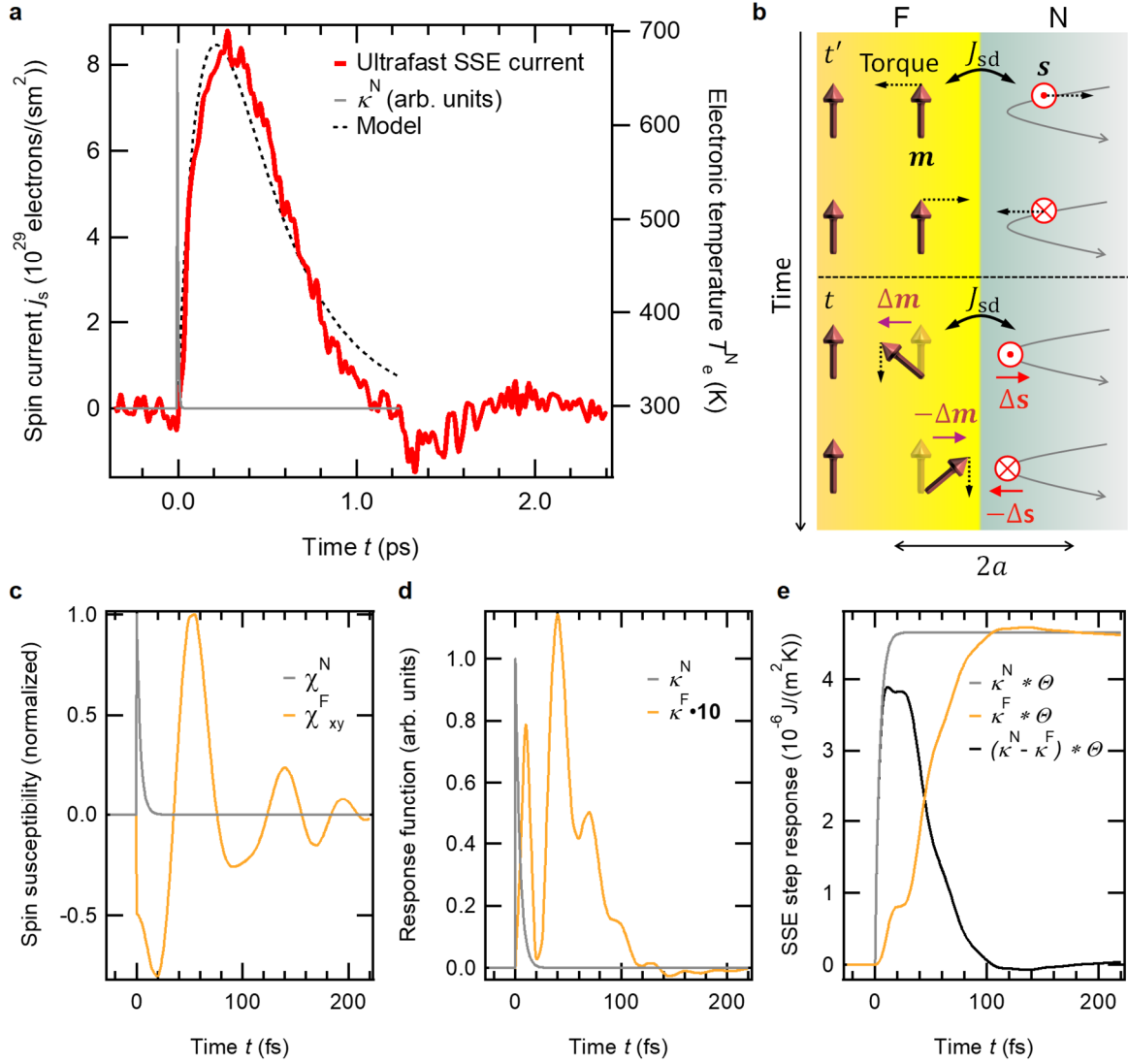


Figure 4 | Femtosecond dynamics of the interfacial spin Seebeck effect. **a**, Extracted density $j_s(t)$ of the spin current entering the Pt layer together with a phenomenological model function $[1 - \exp(-t/\tau_1)] \times \exp(-t/\tau_2)$ with time constants of electron thermalization (τ_1) and cooling (τ_2) taken from literature^{36,37}. **b**, Model schematic of the F|N interface. At time t' , an N electron entering the interaction region induces a fluctuation $s(t')$ of the total N-cell spin. It exerts the effective field $\pm J_{sd}s(t')$ on the F-cell spin for opposite $+s(t')$ and $-s(t')$. Consequently, at a slightly later time t , the F-cell spin changes by $\pm \Delta M(t)$, resulting in zero change of the average F-cell spin. However, a second interaction with the N-cell field leads to the rectified torque $J_{sd}s(t) \times \Delta M(t)$ for both s directions and, thus, a net spin current between F and N. **c**, Calculated time-domain spin susceptibility of the F=YIG cell (transverse $\chi_F^N(t)$) and the N=Pt cell (isotropic $\chi^N(t)$). **d**, Calculated dynamics of the SSE response functions $\kappa^N(t)$ and $\kappa^F(t)$ which quantify, respectively, the spin current induced by a $\delta(t)$ -like temperature increase of the N=Pt and F=YIG layer (see text). For comparison, κ^N is also shown in panel **a**. **e**, Resulting SSE responses $(\kappa^N * \Theta)(t)$ and $(\kappa^F * \Theta)(t)$ (grey and yellow curve, respectively) induced by the same step-like temperature increase $\Theta(t)$ at $t = 0$ in both layers. The total response $(\kappa^N * \Theta - \kappa^F * \Theta)(t)$ is also shown (black curve). To obtain an absolute ordinate scaling in agreement with the experiment, an interfacial exchange constant of $J = 2 \text{ meV}$ was used.

Introduction

The electron spin holds an enormous potential to extend conventional charge-based electronics into spintronics, entailing exciting novel functionalities¹. An important example is the transport of information carried by spin angular momentum. In contrast to charge currents, such spin currents can also flow in magnetic insulators by means of spin waves (magnons). They can be launched, for instance, by applying temperature gradients^{2,3,4}. This spin Seebeck effect (SSE)⁵ is also observed at the interface^{3,6,7} of a magnetic insulator (F) and a nonmagnetic metal (N) (see Fig. 1a). Here, a static temperature difference $T^N - T^F$ induces a spin current with density^{2,8}

$$j_s = K \cdot (T^N - T^F). \quad (1)$$

It is polarized parallel to the F magnetization and can be measured in the N layer through the inverse spin Hall effect (ISHE) which converts the longitudinal j_s into a detectable transverse charge current j_c (Fig. 1a). Magnon accumulation at the F|N interface can make an additional contribution not included in Eq. (1)^{3,9}.

Eq. (1) presumes a static temperature difference and frequency-independent spin Seebeck constant K . It is still open how this relationship should be modified for fast temporal variations of T^N and T^F , for nonthermal states and whether there is a cutoff frequency above which j_s is suppressed. These questions directly address the impact of ultrafast processes such as magnon precession in YIG¹⁰ and spin relaxation in Pt¹¹ on the buildup speed of the SSE current. The high-frequency behavior of the SSE is also highly relevant for applications such as magnetization control by THz spin currents¹² and spintronic THz radiation sources^{13,14,15}.

In previous time-resolved SSE works, a transient $T^N - T^F$ was induced by heating the N layer with an optical or microwave pulse. The transient spin current was detected by measuring either the ISHE voltage up to GHz bandwidth^{6,7,16} or the local spin polarization by magneto-optic probes¹⁷. It was shown that Eq. (1) remains valid on the time resolution of these experiments, that is, from microseconds⁶ through to ~ 0.1 ns⁷ and even down to 1.2 ps¹⁷. These results call for even better time resolution and bandwidth, ultimately reaching the 10 fs/100 THz scale, which is required to resolve even the fastest spin dynamics in magnetic materials¹⁸. For a direct comparison to the majority of SSE works, the spin current should ideally be detected through the ISHE.

In this work, we extend the archetypal longitudinal SSE scheme to the ultrafast/THz regime in the most straightforward way (see Fig. 1a). We excite the metal of YIG|Pt bilayers with laser pulses (duration of 10 fs, center photon energy of 1.6 eV, energy of 3.2 nJ) from a Ti:sapphire laser oscillator (repetition rate of 80 MHz). Any ultrafast spin current $j_s(t)$ arising in the metal is converted into a transverse charge current and acts as a source of an electromagnetic pulse in the terahertz (THz) frequency range. As detailed in the Methods section and Ref. 19, we determine the spin current $j_s(t)$ with a time resolution of 10 fs by contact-free electrooptic detection of the transient THz electric field over a bandwidth of 45 THz. If not mentioned otherwise, measurements are conducted at room temperature in a dry N₂ atmosphere in an external in-plane-oriented magnetic field of 10 mT saturating the YIG magnetization.

Experimental results

Central experimental data are summarized in Figs. 2 and 3. While Fig. 2 displays THz signals for different magnetization directions, metal cap layers and pump powers, Fig. 3 shows the dependence of the THz signal on sample temperature and external magnetic field. We start with Fig. 2a, which presents typical THz electrooptic signals S versus time t for a YIG(3 μ m)|Pt(5.5 nm) bilayer. The signals reverse almost entirely when the in-plane sample magnetization is reversed from $+\mathcal{M}$ to $-\mathcal{M}$. Because we are interested in SSE physics, we focus on the difference $S_- = S(+\mathcal{M}) - S(-\mathcal{M})$ odd in \mathcal{M} in the following.

As seen in Fig. 2b, the root mean square (RMS) amplitude of $S_-(t)$ grows approximately linearly with the pump power. Figure 2c shows the S_- amplitude as a function of the external magnetic field along with the sample magnetization \mathcal{M} measured by the magneto-optic Faraday effect. We find that the THz signal follows the hysteretic magnetization curve perfectly. Additional measurements reveal that the

THz electric field associated with $S_-(t)$ is linearly polarized and oriented perpendicularly to \mathcal{M} (Fig. S2). Furthermore, when changing the layer sequence from F|N to N|F, $S_-(t)$ is found to change polarity (Fig. S3). Also, $S_-(t)$ does not depend on the pump-pulse polarization (linear and helical).

To test the relevance of the ISHE, we change the sign of the spin Hall angle of the N metal by replacing Pt by W. As seen in Fig. 2d, THz signals $S_-(t)$ from YIG|W and YIG|Pt yield opposite sign, and the signal amplitude is smaller for YIG|W, consistent with previous ISHE works^{20,21}. A test measurement on a bare YIG film does not yield any detectable signal $S_-(t)$ (see Fig. S4). These observations and symmetry properties of the THz signal are consistent with the notion that the femtosecond pump pulse injects an ultrafast out-of-plane-directed, \mathcal{M} -polarized spin current into the N layer where it is converted into a transverse charge current by the ISHE (see Fig. 1a).

Figure 2e shows that even upon introducing a 1.9 nm Cu spacer layer between YIG and Pt, a measurable THz signal prevails. Therefore, a possible (Nernst-like) contribution due to proximity-induced Pt magnetic moments at the YIG/Pt interface is negligibly small, in agreement with previous results^{22,21,23}. Likewise, a photo-spin-voltaic effect as reported recently²⁴ does not make a dominant contribution to the THz signal. Our result is fully consistent with the picture of a spin current flowing from YIG to Pt and traversing the Cu layer. The amplitude reduction by ~ 6 as compared to YIG|Pt can be explained by spin-current loss in Cu^{14,25} and the reduced optical excitation density of the thicker metal films¹³.

THz spin Seebeck effect

To reveal the nature of the THz spin current at the YIG|Pt interface, we measure the impact of the equilibrium sample temperature T_0 . Figure 3a displays the bulk magnetization of the YIG(3 μm)|Pt(5.5 nm) sample versus T_0 as measured by the magneto-optic Faraday effect (see Methods). The Faraday signal disappears at $T_0 = 555$ K, consistent with the Curie temperature T_C of bulk YIG. Figure 3b reveals that the RMS amplitude of the THz signal S_- and, thus, the THz spin-current amplitude also decrease with rising T_0 , but more rapidly than the YIG bulk magnetization. Remarkably, for $T < T_C$, the curve can be well described by a function proportional to $(T_C - T_0)^3$, in striking agreement with the recently measured temperature dependence of the SSE/ISHE voltage in static experiments on YIG|Pt bilayers²⁶. We summarize that the THz emission signal S_- exhibits all characteristics of the DC SSE. Therefore, the THz data of Figs. 2 and 3 can be considered as a clear manifestation of the SSE at THz frequencies.

To extract the spin current $j_s(t)$ flowing in the Pt layer of the YIG(3 μm)|Pt(5 nm) sample, we apply an inversion procedure to our THz electrooptic signal waveforms¹⁹. Figure 4a shows the central experimental result of this study: the ultrafast dynamics of the SSE current following excitation by a 10 fs laser pulse. Strikingly, j_s rises on an ultrafast time scale of 100 fs, more than one order of magnitude shorter than interfacial SSE response times reported so far for laser-heated YIG|Pt^{6,7,16,17}. The positive sign of j_s implies that the magnetization of YIG decreases (see Fig. S5).

Model of the dynamic spin Seebeck effect

To gain insight into the ultrafast rise and relaxation of the SSE current, we adapt the model picture³ of the static SSE to the dynamic case and employ the linear-response approach to spin pumping^{27,28}. A model schematic is shown in Fig. 4b: according to *ab initio* calculations²⁹, the spins of the interfacial F and N layers are coupled by an sd-type Hamiltonian $J_{sd}\mathbf{M} \cdot \mathbf{S}$ over a thickness that equals about one lattice constant $a = 1.24$ nm of YIG. Here, J_{sd} is an effective coupling constant, and $\hbar\mathbf{M}$ and $\hbar\mathbf{S}$ are the total electron spin angular momentum contained in an interfacial cell of dimension a^3 on the F and N side, respectively. Thermal spin fluctuations $\mathbf{m}(t)$ in F and $\mathbf{s}(t)$ in N cause stochastic effective magnetic fields $J_{sd}\mathbf{m}(t)$ and $J_{sd}\mathbf{s}(t)$ and, therefore, torque of F on N and vice versa, respectively. As a result, spin currents j_s^F and j_s^N flow, which cancel each other for $T^F = T^N$.

In our experiment, this balance is perturbed by the pump pulse exciting exclusively the N electrons. Consequently, we focus on elementary interactions and the current j_s^N caused by spin fluctuations in N, as illustrated in Figs. 4b and 4c and derived rigorously in the Methods section. At time t' (Fig. 4b), the conduction electrons in the N cell exert the random field $J_{sd}\mathbf{s}(t')$ on the F-cell spins³. Therefore, at a slightly later time $t > t'$, the F-cell spin has changed dynamically by

$\Delta \mathbf{m}_i(t) = \sum \chi_{ij}^F(t-t') J_{sd} \mathbf{s}_j(t')$ where χ_{ij}^F is the spin susceptibility tensor of the F cell in the time domain^{3,27} (Fig. 4c). On average, however, this interaction does not result in a spin current because the expectation value $\langle \mathbf{s} \rangle$ of the spin fluctuation of N is zero (Fig. 4b).

Nevertheless, a net effect can be achieved by a second interaction of F with $J_{sd} \mathbf{s}$ at time $t > t'$. The resulting torque $J_{sd} \mathbf{s}(t) \times \Delta \mathbf{m}(t)$ scales with J_{sd}^2 and, therefore, rectifies the random field $J_{sd} \mathbf{s}$. Its expectation value is parallel to the F magnetization \mathcal{M} (Fig. 4b). To obtain the spin current due to the N fluctuations, we integrate the second-order torque over all first-interaction times t' and find

$$j_s^N(t) = \frac{J_{sd}^2}{a^2} \int dt' \chi_{\perp}^F(t-t') \langle s_z(t) s_z(t') \rangle. \quad (2)$$

Equation (2) provides the key to understanding the dynamics of the SSE. The spin correlation function $\langle s_z(t) s_z(t') \rangle$ shows that average torque on the F spins only arises if the two interactions with $J_{sd} \mathbf{s}$ occur within the correlation time τ^N of the N-cell spin. Since the fluctuations $s_z(t)$ predominantly arise from the electrons entering and leaving the N cell^{5,30,31}, τ^N can be estimated by the time it takes an electron to traverse the N cell (Fig. 4b). By averaging the Fermi velocity³² over all angles of incidence, we obtain $\tau^N \sim 3.5$ fs. Once the pump pulse excites the N electrons, their distribution function changes abruptly. The spin correlation function follows these modifications on a 3.5 fs time scale, faster than the pump-pulse duration of 10 fs. Interestingly, the F spins react even instantaneously because ferromagnetically coupled spins are known to have no inertia³³. Consequently, the transverse susceptibility $\chi_{\perp}^F(t) = \chi_{xy}^F(t) - \chi_{yx}^F(t)$ of the F-cell starts step-like at $t = 0$ (Fig. 4c), and the spin current rises on ultrafast time scales, consistent with our experimental observation (Fig. 4a).

The strength of the spin fluctuations in the N cell is proportional to the frequency at which Pt conduction electrons scatter off the F|N interface (Fig. 4b). Assuming elastic and diffuse scattering, this rate scales with the number of occupied incident and unoccupied outgoing Bloch states, that is, with the quantity

$$\tilde{T}_e^N(t) = \frac{1}{k_B} \int d\epsilon n(\epsilon, t) [1 - n(\epsilon, t)]. \quad (3)$$

Here, $n(\epsilon, t)$ is the occupation number of a state at electron energy ϵ (see Methods). Interestingly, when $n(\epsilon, t)$ is given by the Fermi-Dirac function at temperature $T_e^N(t)$, we obtain $\tilde{T}_e^N(t) = T_e^N(t)$, thereby identifying $\tilde{T}_e^N(t)$ as a generalized electronic temperature. Using this result and the Kubo formula, we can express the correlation $\langle s_z(t) s_z(t') \rangle$ by means of \tilde{T}_e^N and the isotropic spin susceptibility χ^N of the N cell. Equation (2) then yields the spin current

$$j_s(t) = \int dt' \kappa^N(t-t') \tilde{T}_e^N(t') \quad (4)$$

due to the fluctuations of the N spins. This relationship is the desired generalization of Eq. (1) for time-dependent N temperatures and nonthermal electron distributions.

The response function $\kappa^N(t) = k_B J_{sd}^2 a^{-2} \chi_{\perp}^F(t) \int_t^{\infty} dt' \chi^N(t')$ is entirely given by the susceptibilities of the F- and N-cell spins. To calculate its dynamics for our F=YIG|N=Pt sample system, we assume an isotropic Pauli-type susceptibility³⁴ $\chi^N(t)$ with step-like increase and exponential decay with time constant τ^N (see Fig. 4c). In contrast, $\chi_{\perp}^F(t)$ is determined by classical atomistic spin-dynamics simulations^{10,35} and exhibits a strongly damped oscillation because many magnon modes contribute to the spin dynamics of the F cell in YIG (see Methods and Fig. 4c). The resulting $\kappa^N(t)$ is displayed in Fig. 4d. It has an ultrashort peak-like shape with a very small width on the order of τ^N , consistent with our qualitative discussion following Eq. (2).

Discussion

Since $\kappa^N(t)$ is much narrower than the rising edge of the measured spin current $j_s(t)$ (see Fig. 4a), the evolution of j_s must arise from the dynamics of the laser-excited Pt electrons. Indeed, the rise and

decay times of the measured $j_s(t)$ agree remarkably well with the time constants $\tau_1 = 0.26$ ps and $\tau_2 = 0.36$ ps, respectively, with which the photoexcited electrons in Pt are known to approach a Fermi-Dirac distribution³⁶ and to transfer their excess energy to the cold lattice³⁷.

Therefore, we ascribe the ultrafast temporal rise and decay of the SSE current to the thermalization and cooling of the optically excited Pt electrons, as supported by the following arguments. First, we phenomenologically model the dynamics of the spin current by $[1 - \exp(-t/\tau_1)] \cdot \exp(-t/\tau_2)$. As seen in Fig. 4a, we find excellent agreement between the model function and the measured $j_s(t)$, without any fit parameters. Second, we observe almost identical relaxation dynamics of ultrafast spin current and transient optical reflectance, which is known to approximately monitor the decay of the electron temperature^{17,37} (see Methods and Fig. S6).

Third, according to Eq. (3), maximum spin current is achieved when the pump pulse pushes the electronic occupation number $n(\epsilon, t)$ toward a value of 0.5 over an electron-energy range as large as possible. Therefore, as many electron-hole pairs as possible should be generated for a given deposited pump-pulse energy. Initially, photoexcitation induces electrons and holes on average at half the pump photon energy of $\hbar\omega_p = 1.6$ eV above and below ϵ_F , respectively. However, on a time scale given by τ_1 , electron-electron scattering cascades multiply the number of electrons and holes by a factor on the order of $\hbar\omega_p/k_B T_e^N \sim 30$. Consequently, the generalized temperature $\tilde{T}_e^N(t)$ and the spin current increase with time constant τ_1 . The rise of the measured $j_s(t)$ can be considered as an experimental confirmation of the notion that the SSE current is due to electrons impinging on the YIG|Pt interface. We note that we have added a temperature scale on the right ordinate of Fig. 4a whose peak value is determined by the absorbed pump-pulse energy density and the Pt electronic specific heat³⁸.

It is interesting to consider the peak ISHE electric field normalized by the peak temperature increase $T_e^N - T_0$ (Fig. 4a), which yields an efficiency figure of ~ 1 V m⁻¹ K⁻¹. This value is on the same or similar order of magnitude as results from SSE experiments on samples with Pt layers of similar thickness, both for static (0.1 V m⁻¹ K⁻¹)³⁹ and laser-heating at MHz (0.7 V m⁻¹ K⁻¹)⁶ and GHz frequencies (37 V m⁻¹ K⁻¹)⁷. Comparison of the efficiency found in our work to our modeling yields an estimate of the YIG/Pt interfacial exchange coupling constant of $J_{sd} \sim 2$ meV. This value approximately agrees with the antiferromagnetic exchange coupling constant J_{ad} between adjacent a-Fe³⁺ and d-Fe³⁺ ions of bulk YIG.⁴⁰ It can be converted into a spin mixing conductance with real part $\text{Re } g^{\uparrow\downarrow} = 5 \times 10^{18}$ m⁻², which is in good agreement with calculated²⁹ and measured values^{41,42}.

To estimate how strongly the YIG is modified by the ultrafast spin current, we time-integrate the measured $j_s(t)$ (Fig. 4a). The resulting loss of spin angular momentum is equivalent to increasing the temperature of the interfacial YIG monolayer by about 50 K (Fig. 3a), which is one order of magnitude less than the increase of the Pt electron temperature T_e^N . This small effect is further diminished by transport of magnons away from the interface. Therefore, we can neglect any significant back-action of the heated YIG layer on the spin current.

So far, our experiments have been restricted to excitation of the metal part of YIG|Pt. Our modeling, however, allows us to also calculate the SSE response function $\kappa^F(t)$ related to heating of the F=YIG layer (see Fig. 4d and Methods). If a fictitious sudden and uniform temperature jump were applied simultaneously to both YIG and Pt layers, no current would flow according to Eq. (1). In contrast, our theory predicts a short current burst with a duration of about 100 fs (Fig. 4e). It arises from the inherent asymmetry of the F|N structure. At times $t > 100$ fs, the total spin current vanishes, consistent with the familiar static result of Eq. (1).

Conclusion

We observe an ultrafast charge current in prototypical YIG|Pt bilayers triggered by femtosecond optical excitation of the metal layer. It features all the hallmarks expected from the THz analogue of the SSE in terms of symmetries, sample structure and sample temperature. Our modeling, based on exchange-coupled YIG|Pt layers, delivers an order of magnitude and rise time of the photocurrent that are both fully consistent with our experimental observations. In particular, the femtosecond response is found to arise from the ultrashort spin correlation time of the heavy metal and the inertia-free, almost step-like transverse response of the YIG spins.

These results are significant. In terms of applications, the ultrafast SSE current of Fig. 4a can be understood as a first demonstration of incoherent THz spin pumping. Therefore, an instantaneously heated metal layer is a promising transducer for launching ultrashort THz magnon pulses into YIG. They may lend themselves for magnon-based information transfer and for exerting torque on remote magnetic layers.

From a fundamental viewpoint, our experimental approach permits characterization of the interfacial SSE and the ISHE of metals in standard bilayer thin-film stacks, without extensive micro structuring and contacting. Likewise, the THz interfacial SSE can be considered a contact-free probe of the magnetic texture and the exchange coupling at interfaces. As indicated by Eq. (2), the THz SSE current can also be used to measure local electron spin noise at highest frequencies, even under highly transient, nonstationary conditions. Finally, the YIG|Pt bilayer studied here serves as a model system for all magnetic systems in which laser-driven spin transfer between two constituents (such as alloy components⁴³ and spin sublattices⁴⁴) plays a significant role.

References

- ¹ Sander, D., et al. "The 2017 Magnetism Roadmap." *J. Phys. D: Appl. Phys.* **50** (2017): 363001.
- ² Bauer, Gerrit EW, Eiji Saitoh, and Bart J. Van Wees. "Spin caloritronics." *Nature materials* **11** (2012): 391-399.
- ³ Adachi, Hiroto, et al. "Theory of the spin Seebeck effect." *Reports on Progress in Physics* **76** (2013): 036501.
- ⁴ Chumak, A. V., et al. "Magnon spintronics." *Nature Physics* **11** (2015): 453-461.
- ⁵ Uchida, K., et al. "Spin Seebeck insulator." *Nature materials* **9** (2010): 894-897.
- ⁶ Agrawal, M., et al. "Role of bulk-magnon transport in the temporal evolution of the longitudinal spin-Seebeck effect." *Physical Review B* **89** (2014): 224414.
- ⁷ Schreier, Michael, et al. "Spin Seebeck effect at microwave frequencies." *Physical Review B* **93** (2016): 224430.
- ⁸ Xiao, Jiang, et al. "Theory of magnon-driven spin Seebeck effect." *Physical Review B* **81** (2010): 214418.
- ⁹ Rezende, S. M., et al. "Magnon spin-current theory for the longitudinal spin-Seebeck effect." *Physical Review B* **89** (2014): 014416.
- ¹⁰ Barker, Joseph, and Gerrit EW Bauer. "Thermal spin dynamics of yttrium iron garnet." *Physical review letters* **117** (2016): 217201.
- ¹¹ Freeman, Ryan, et al. "Intrinsic and extrinsic contributions to spin scattering in Pt." *arXiv preprint arXiv:1707.05330* (2017).
- ¹² Schellekens, A. J., et al. "Ultrafast spin-transfer torque driven by femtosecond pulsed-laser excitation." *Nature communications* **5** (2014): 4333.
- ¹³ Seifert, T., et al. "Efficient metallic spintronic emitters of ultrabroadband terahertz radiation." *Nature Photonics* **10** (2016): 483-488.
- ¹⁴ Wu, Yang, et al. "High-Performance THz Emitters Based on Ferromagnetic/Nonmagnetic Heterostructures." *Advanced Materials* **29** (2017).
- ¹⁵ Yang, Dewang, et al. "Powerful and tunable THz emitters based on the Fe/Pt magnetic heterostructure." *Advanced Optical Materials* **4** (2016): 1944-1949.
- ¹⁶ Bartell, Jason M., et al. "Imaging Magnetization Structure and Dynamics in Ultrathin Y 3 Fe 5 O 12/Pt Bilayers with High Sensitivity Using the Time-Resolved Longitudinal Spin Seebeck Effect." *Physical Review Applied* **7** (2017): 044004.
- ¹⁷ Kimling, Johannes, et al. "Picosecond spin Seebeck effect." *Physical review letters* **118** (2017): 057201.
- ¹⁸ Kirilyuk, Andrei, Alexey V. Kimel, and Theo Rasing. "Ultrafast optical manipulation of magnetic order." *Reviews of Modern Physics* **82** (2010): 2731.

-
- ¹⁹ Braun, Lukas, et al. "Ultrafast photocurrents at the surface of the three-dimensional topological insulator Bi₂Se₃." *Nature communications* **7** (2016): 13259.
- ²⁰ Sinova, Jairo, et al. "Spin hall effects." *Reviews of Modern Physics* **87** (2015): 1213.
- ²¹ Guo, Er-Jia, et al. "Influence of thickness and interface on the low-temperature enhancement of the spin Seebeck effect in YIG films." *Physical Review X* **6** (2016): 031012.
- ²² Geprägs, Stephan, et al. "Investigation of induced Pt magnetic polarization in Pt/Y₃Fe₅O₁₂ bilayers." *Applied Physics Letters* **101** (2012): 262407.
- ²³ Kikkawa, T., et al. "Longitudinal spin Seebeck effect free from the proximity Nernst effect." *Physical review letters* **110** (2013): 067207.
- ²⁴ Ellsworth, David, et al. "Photo-spin-voltaic effect." *Nature Physics* **12** (2016): 861-866.
- ²⁵ Du, Chunhui, et al. "Enhancement of pure spin currents in spin pumping Y₃Fe₅O₁₂/Cu/metal trilayers through spin conductance matching." *Physical Review Applied* **1** (2014): 044004.
- ²⁶ Uchida, Ken-ichi, et al. "Quantitative temperature dependence of longitudinal spin Seebeck effect at high temperatures." *Physical Review X* **4** (2014): 041023.
- ²⁷ Šimánek, E., and B. Heinrich. "Gilbert damping in magnetic multilayers." *Physical Review B* **67** (2003): 144418.
- ²⁸ Tserkovnyak, Yaroslav, et al. "Nonlocal magnetization dynamics in ferromagnetic heterostructures." *Reviews of Modern Physics* **77** (2005): 1375.
- ²⁹ Jia, Xingtao, et al. "Spin transfer torque on magnetic insulators." *EPL (Europhysics Letters)* **96** (2011): 17005.
- ³⁰ Silsbee, R. H., A. Janossy, and P. Monod. "Coupling between ferromagnetic and conduction-spin-resonance modes at a ferromagnetic—normal-metal interface." *Physical Review B* **19** (1979): 4382.
- ³¹ Kajiwara, Y., et al. "Transmission of electrical signals by spin-wave interconversion in a magnetic insulator." *Nature* **464** (2010): 262.
- ³² Ketterson, J. B., et al. "Fermi velocity and Fermi radius in platinum." *Solid State Communications* **6** (1968): 851-854.
- ³³ Kimel, A. V., et al. "Inertia-driven spin switching in antiferromagnets." *Nature Physics* **5** (2009): 727.
- ³⁴ Clogston, A. M., V. Jaccarino, and Y. Yafet. "Interpretation of Knight shifts and susceptibilities of transition metals: Platinum." *Physical Review* **134** (1964): A650.
- ³⁵ Ellis, Matthew OA, et al. "The Landau–Lifshitz equation in atomistic models." *Low Temperature Physics* **41** (2015): 705-712.
- ³⁶ Lei, C., et al. "Hot-electron-driven charge transfer processes on O₂/Pt (111) surface probed by ultrafast extreme-ultraviolet pulses." *Physical Review B* **66** (2002): 245420.
- ³⁷ Caffrey, Andrew P., et al. "Thin film non-noble transition metal thermophysical properties." *Microscale Thermophysical Engineering* **9** (2005): 365-377.
- ³⁸ Gray, Dwight E. *American institute of physics handbook*. McGraw-Hill, 1982.
- ³⁹ Kehlberger, Andreas, et al. "Length scale of the spin Seebeck effect." *Physical review letters* **115** (2015): 096602.
- ⁴⁰ Cherepanov, Vladimir, Igor Kolokolov, and Victor L'vov. "The saga of YIG: spectra, thermodynamics, interaction and relaxation of magnons in a complex magnet." *Physics reports* **229** (1993): 81-144.
- ⁴¹ Burrowes, Capucine, and Bretislav Heinrich. "Spin Pumping at Yttrium Iron Garnet Interfaces." *Magnonics*. Springer Berlin Heidelberg, 2013. 129-141.
- ⁴² Weiler, Mathias, et al. "Experimental test of the spin mixing interface conductivity concept." *Physical review letters* **111** (2013): 176601.
- ⁴³ Kirilyuk, Andrei, Alexey V. Kimel, and Theo Rasing. "Laser-induced magnetization dynamics and reversal in ferrimagnetic alloys." *Reports on progress in physics* **76** (2013): 026501.
- ⁴⁴ Tveten, Erlend G., Arne Brataas, and Yaroslav Tserkovnyak. "Electron-magnon scattering in magnetic heterostructures far out of equilibrium." *Physical Review B* **92** (2015): 180412.